sciendo

DOI 10.2478/ama-2023-0046

acta mechanica et automatica, vol.17 no.3 (2023)
Special Issue "Modeling and experimental investigations of thermo-hydraulic, hydrogen, manufacturing and mechanical systems"

AERODYNAMIC INVESTIGATION ON THE ARTEFACT "BIRD OF SAQQARA"

Michel ZIEROW*, Leon LESEMANN*

*City University of Applied Sciences, Faculty of Nature and Engineering,
Institute of Aerospace Technology, Flughafenallee 10, 28199 Bremen, Germany

michelzierow@gmail.com, leonlesemann@gmail.com

received 9 October 2022, revised 4 April 2023, accepted 4 April 2023

Abstract: Lost, technical knowledge of ancient cultures is being rediscovered in modern times during archaeological excavations. A presumed example of the innovative power of ancient cultures is the artefact "Bird of Saqqara". In the context of this paper, the aerodynamic characteristics of the artefact are to be determined by a computational fluid simulation, in order to be able to make a statement about the actual flight suitability and to examine the theses of the pre-astronautics critically. Based on a 3D scan, a CAD model of the artefact is created and then a numerical flow simulation is performed. By varying the angle of attack, the dimensionless coefficients can be represented in corresponding polars. The results show that the artefact has a low maximum glide ratio and thus the glide properties are not sufficient for use as a handglider. The centre of gravity of the artefact is located at the trailing edge of the wing and behind the neutral point. The resulting longitudinal stability does not meet modern specifications. Asymmetric lift distribution in the spanwise direction results in uncontrolled roll. Consequently, the artefact cannot fly a straight path. Within the scope of this work, the connection between the "Bird of Saqqara" and an alleged knowledge of aerodynamics in ancient Egypt could not be confirmed.

Key words: Saqqara, bird, aerodynamics, archaeology, CFD, flight mechanics, Paleo-SETI, Egypt, Ancient Aliens

1. INTRODUCTION

Through findings and archaeological excavations in modern times, mankind continues to discover the advanced and highly technological knowledge that ancient cultures already possessed. To determine whether the findings are actually based on early inventive genius and knowledge of correlation, extensive research must be carried out. Thus, it happens that in the case of some ancient objects discovered by archaeological excavation, only assumptions can be made, which are taken up by pseudo-sciences and conspiracy theories. One of these pseudo-sciences is the so-called ancient-astronautics, which brings the alleged technical progress of some cultures into a connection with claims for the legitimacy of theories positing the existence of extraterrestrial life forms. The conspiracy theories refer to ancient religious writings or archaeological finds whose presumed purpose conflicts with the technical possibilities of the time of origin. One of these finds is the so-called "Bird of Saqqara", a wooden figure allegedly resembling a modern high-winged airplane. In pre-astronautics, this artefact is considered to indicate knowledge of aerodynamic and flight mechanics. In the context of this paper the aerodynamic characteristics of the artefact are to be determined by a computational fluid simulation, in order to be able to make a statement about the actual flight suitability and to examine the theses of the pre-astronautics critically.

2. INVESTIGATION OF THE ARTEFACT USING CFD SIMULATION

This section will describe the execution of the simulation with all associated work steps. For this purpose, the transfer of the scan file into a suitable file format and the associated simplifications and abstractions are described first. Subsequently, the creation and optimisation of the mesh, as well as the setting of the solution parameters, will be discussed. The mathematical and flight-mechanical basics will not be explained further within this paper.

2.1. Pre-processing

A 3D photoscan of the artefact, which was created by Mr. Maximilian Schecker and the staff of the Egyptian Museum in Cairo, serves as the basis for the flow simulation in Ansys Fluent 2020 R1. The point cloud, which is in .fbx format, is subjected to reengineering to convert the scan file into a solid and prepare it for a computional fluid dynamics (CFD) simulation. The process mainly consists of the following steps (conducted in this order):

- Modifying the scan file
- Converting the scan file format to a computer aided design (CAD) exchange format
- Scaling the CAD model to the original size
- Introduction of a body-fixed coordinate system
- Mapping the fuselage and wing through multiple section planes
- Transferring the sectional sketches to a new CAD model
- Creating a solid for the fuselage and wing
- Merging the individual parts into an assembly
- Prepare the assembly for a CFD simulation in Ansys SpaceClaim 2020 R1

In addition to the artefact, the original scan file still contains the pedestal of the model on which it is presented in the Egyptian Museum. This is removed in the first step using Autodesk Fu-

DOI 10.2478/ama-2023-0046

sion360 software to limit the amount of computing capacity required to process the model. The file is then converted into a surface model in .STEP-format and exported so that it can be further processed with more extensive CAD software.

The processing then takes place in Autodesk Inventor Professional 2022. Since scaling errors can occur during transfer to a CAD exchange format, the model first is scaled to its correct dimensions in Inventor. This is done by referring to drawings made by Messiha [1], although the exact dimensions are not decisive for the dimensionless coefficients. Due to the high level of detail of the 3D scan, it is not possible to convert the surface model directly into a solid in Inventor.

This goal can be achieved by cutting the fuselage and the wing of the bird into up to 44 partial segments and mapping the contour of the body in the cutting plane on each cut surface by means of a spline. To be able to transfer the resulting sectional surfaces to a separate CAD model and convert them there into a solid model, the sketches must be aligned with a common coordinate system. For this purpose, a longitudinal (Y), vertical (Z) and lateral (X) axis is added to the model (see Fig. 1).

Subsequently, 44 cutting planes are placed in the fuselage and 30 in the wing, on which the contour of the cross section is reproduced. The distance between the cutting planes is not specified with a constant value, but adjusted according to the curvature of the geometry. Finally, the cutting planes are connected to each other via an elevation so that a separate solid is created for the wing and fuselage, which get positioned in relation to each other in an assembly.

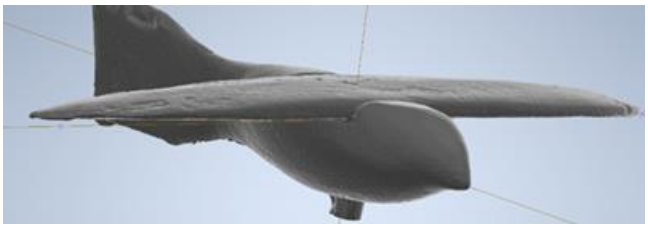

Fig. 1. STEP-file with additional coordinate system

Before the model could be subjected to a flow simulation, the simulation environment had to be defined in its geometry via Ansys SpaceClaim 2020. Accordingly, a higher resolution region in the near field of the artefact, a so-called body of influence (BOI), is also created. The simulation environment has dimensions of $1{,}240.95\ \text{mm} \times 1{,}032.74\ \text{mm} \times 1{,}178\ \text{mm}$, and the BOI is defined as $374.66\ \text{mm} \times 181\ \text{mm} \times 350\ \text{mm}$. In addition, the geometries get named via so-called named selections in order to be able to determine the flow inlet, the flow outlet and the artefact in the simulation software in the further course.

By exporting the file as .tgf, the computational grid can be generated in Ansys Fluent.

2.2. Generation of the mesh

An important step in CFD simulation is the discretisation of the differential equations by a mesh. First, a surface grid is generated for this purpose, which is then to be converted into a volume grid. For the surface grid, the cells are generated finer by applying the so-called sizings for certain regions. The goal is to effectively resolve the cell regions where high gradients of the flow variables are expected. On the surface of the object, the sizing curvature is used, in which the cells are made finer at higher curvature of the surface. In addition, the cells on the surface of the BOI are generated finer than the global cell dimensions using the sizing of the corresponding name to better resolve the flow-field near the object. The far field of the flow is globally resolved coarser than the other regions, since high gradients of flow variables are not expected in that region. The parameters used to create the surface grid can be found in Tab. 1. By applying various optimisation mechanisms, it is possible to reduce the skewness of the grid to <0.6 in all regions. Thus, the surface grid has a sufficiently high quality. According to the workflow from Ansys Fluent, the volume regions are then computed. Poly-hexcore is used as cell type to reduce the memory usage. In addition, prism cells are used in the boundary layer of the artefact in order to resolve the high gradients normal to the surface well. Since the SST-kω model is to be used for computation afterwards, the standardised wall distance has to be $y^+ \approx 1$ when generating the prism cells [2]. For this purpose, three iteration steps were performed, in which the height of the first layer of prism cells was varied. The number of layers was adjusted so that the total height remained constant. In the third iteration step, this goal was achieved. In addition, various optimisation mechanisms are again applied to optimise the mesh quality. Using the aspect ratio and the inverse orthogonal quality, the mesh quality is finally evaluated as high.

Tab. 1. Parameters of mesh-cells for different sizings

Sizing	Parameter	Values
Global	Min. size	0.1
	Max. size	25
	Growth rate	1.2
BOI (Body of influence)	Min. size	0.1
	Max. size	2.5
	Growth rate	1.2
Curvature	Min. size	0.1
	Max. size	2.5
	Growth rate	1.2
	Normal angle	9°

2.3. Setup of the solver

To set up the solver, the Ansys "Prepare to solve" function first applied several automated changes to the mesh to minimise the subsequent computational effort and fasten the convergence of the results.

As a first step, the boundary surfaces of the enclosure are assigned to the respective functions in the simulation. The leading face acts as a velocity inlet with an inflow velocity of 10 m/s. The airflow at different angles of attack is achieved by varying the directional components. The outflow surface behind the artefact is defined as a pressure outlet with a gauge pressure of 0 MPa. The remaining surfaces of the enclosure retain the type "Wall" and get set to be frictionless.

Report definitions for drag, lift and moment coefficients are generated to determine the coefficients. The reference values required for scaling are the projected wing area (as reference area) and inflow velocity (as reference velocity). As a discretisation method, a second-order method is used for the pressure

sciendo
DOI 10.2478/ama-2023-0046
acta mechanica et automatica, vol.17 no.3 (2023)
Special Issue "Modeling and experimental investigations of thermo-hydraulic, hydrogen, manufacturing and mechanical systems"

equations and the second-order-upwind method is used for the equations of momentum, turbulent kinetic energy and specific dissipation, so that the flow direction is also taken into account in the calculations. To accelerate the convergence of the solutions, explicit relaxation factors (sub-relaxation) are partially applied for the flow variables. As an additional implicit relaxation method, the calculation will be conducted as pseudo-transient.

To avoid the use of wall functions, the SST-kω-model (Reynolds averaged navier stokes equations, RANS-method) is chosen for the calculation [2]. The results are assumed to be converged once the residuals have decreased by approximately three orders of magnitude.

3. EVALATION OF THE SIMULATION RESULTS

In this section, the results of the CFD simulation are evaluated and characterised in order to make a determination about the glide characteristics and the flight performance of the artefact.

3.1. Polars

Computational fluid simulation in a range of angles of attack from $-5°$ to $14°$ in $1°$ steps allows the aerodynamic coefficients of the artefact to be determined. The results are presented in polars.

The lift coefficient shows a linear course in the angle of attack range from $-5°$ to $7°$, reaches a maximum of $c_L = 0.4728$ at $9°$ and decreases with increasing angle of attack due to a progressive stall.

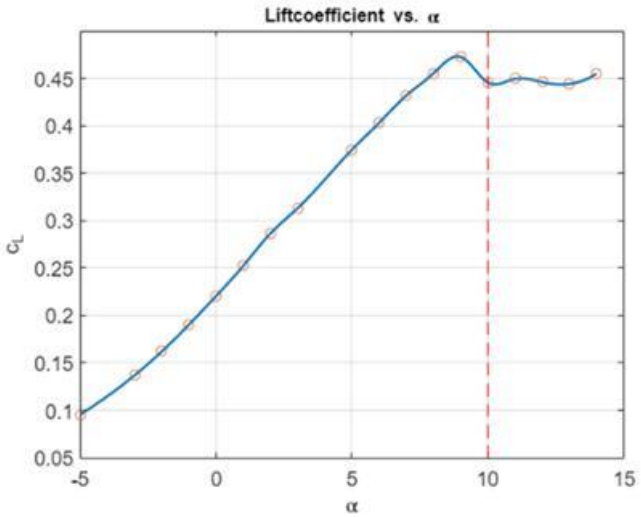

Fig. 2. Lift polar

The polar curve (see fig. 2 and fig. 3) shows that the flow breaks off even at a low angle of attack. Also, no particularly high maximum lift coefficient is achieved. In comparison, a NACA 0012 airfoil achieves a maximum lift coefficient of $c_L \approx 0.9$ [2]. However, the artefact achieves positive lift coefficients even at negative angles of attack, which is due to the twisting of the airfoil in the spanwise direction.

Plotting the lift coefficient versus drag coefficient shows that the artefact has a high parasite drag coefficient of $c_{D,0} = 0.1065$. In comparison, general aviation aircrafts have zero parasite drag coefficients of approximately $c_{D,0} = 0.02 \text{ to } 0.05$ [3]. The high zero drag coefficient is due to the low curvature of the wings leading edge, which can also be seen in the pressure distribution in Fig. 7.

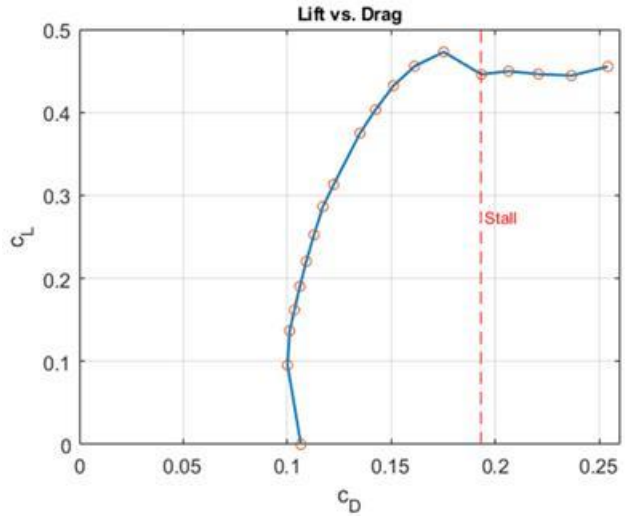

Fig. 3. Lift over drag polar

The combination of high drag coefficients and simultaneously low lift coefficients leads to a maximum lift/drag ratio of only $E_{max} = 2.86$ at an angle of attack of $7°$ on the artefact. The artefact thus does not exhibit good glide characteristics. However, the glide characteristics of the flying object are decisive for engine-less, stationary straight flight, since a high drag cannot be compensated with an engine thrust.

3.2. Flight mechanics calculation

To illustrate the simulation results, simple flight mechanics calculations are conducted. The artefact is assumed to be a mass point and the moment budget is neglected.

For this purpose, the minimum airspeed for engine-less, steady-state glide is first calculated for different flight path angles and angles of attack. In this case, at an angle of attack of 10°, the minimum airspeed for flight path angles from 10–20° is ≈17 m/s. This speed is significantly too high, for a stable, targeted launch by hand.

In addition, the maximum range (launch at best glide angle) and endurance (launch at minimum sink rate) are calculated for a drop from a height of 2 m. The maximum range is 5.48 m and the maximum endurance is 1.51 s. These values underline the poor glide characteristics derived from the polar axis and suggest that the object was not used as a hand glider.

3.3. Position of the centre of gravity and the aerodynamic centre

The derivative $\frac{\delta c_m}{\delta c_\alpha}$ is considered an essential stability measure. Thereby, the moment coefficient must decrease in case of a lift coefficient increase. Since the coefficient is usually nega-

DOI 10.2478/ama-2023-0046

tive, it must increase in magnitude. Consequently, the pitching moment also increases, so that the pitch angle is reduced (stable behaviour) [4]. As shown in Fig. 4, the derivative is positive and therefore does not lead to flight stability.

In addition to the derivative $\frac{\delta c_m}{\delta c_\alpha}$, the position of the centre of gravity and aerodynamic centre (relative to each other) is used to assess flight stability. In this case, the centre of gravity is determined by the CAD model, whereas the aerodynamic centre can be calculated using the stability measure relative to a reference point. The neutral point should be located behind the centre of gravity, at $\approx 15\ \%$ of the reference wing depth, for good flight stability in a wing-fuselage combination [5].

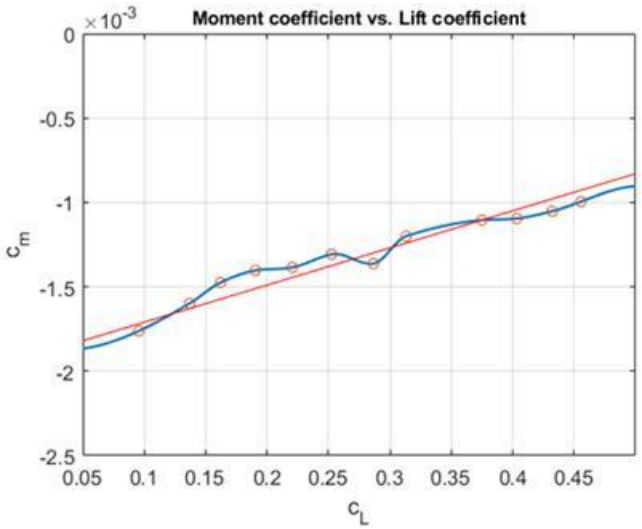

Fig. 4. Moment coefficient versus lift coefficient

The centre of gravity of the artefact is located shortly before the trailing edge of the wing ($54\ \mathrm{mm}$ behind the nose tip) and thus clearly too far to the rear. The calculation of the aerodynamic centre shows that it is located in front of the centre of gravity and also too far in the rear. These characteristics do not indicate sufficient longitudinal stability, which means that the already poor glide characteristics of the artefact cannot be achieved in reality. The position of the centre of gravity and aerodynamic centre is shown in Fig. 5.

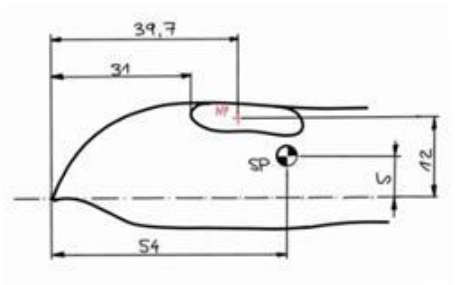

Fig. 5. Position of centre of gravity (SP) and the aerodynamic centre (NP); dimensions in millimetre

3.4. Distribution of pressure and velocity

After the characteristic aerodynamic values of the artefact have been determined and classified in the previous subsection, the curves of pressures and velocities are now to be considered in order to describe the behaviour of the flow. The angles of attack 6° and 11° are considered, since a stall can be assumed between these angles.

The static pressure along the wing at the artefact is roughly similar to that at a typical airfoil (see Fig. 6).

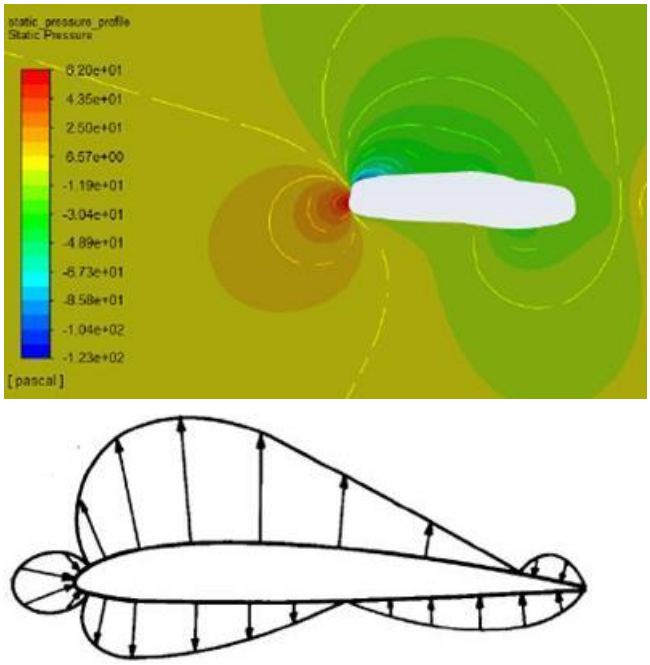

Fig. 6. Pressure distribution (top) and typical pressure distribution of an airfoil (bottom) [4]

Accordingly, a larger area of high static pressure is present at the leading edge of the artefact (shown in Fig. 6), which results from the low curvature of the wings leading edge. Static pressures of up to $p_{stat} = 52\ \mathrm{Pa}$ occur here. Due to the different flow velocities, the static pressure on the upper side of the wing is lower than that on the lower side. Thus, as in the case of classic airfoils, it can be called a suction side. The values here are around $-45\ \mathrm{Pa}$, reaching up to $-123\ \mathrm{Pa}$ in the front area of the profile.

The pressure distribution in the spanwise direction is shown in Fig. 7. As expected, the static pressure decreases in the direction of the wing tips. An asymmetry in the pressure distribution can be seen, with a larger pressure difference at the left wing (from the bird's perspective). This is particularly evident at the left wing tip, with a high overpressure.

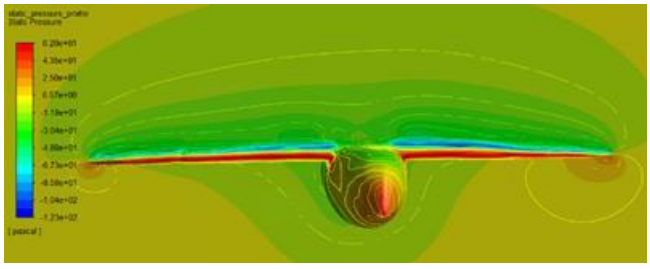

Fig. 7. Spanwise pressure distribution

It is expected that the asymmetric pressure or lift distribution

will cause the artefact to roll, with the right wing tilting downward. Since the total lift vector thus has an additional horizontal component, the bird would fly a right turn. Due to a lack of rudder, coordinated turn flight is not possible, resulting in a bank angle. After the initiation of the roll motion, the angle of bank would steadily increase, and at the same time the artefact, due to its pitching moment balance, would continue to pitch up. This non-stationary flight behaviour leads to a stall and thus to a crash of the bird.

Flow separation phenomena can be investigated by examining the velocity distribution along the wing depth. Similar to the pressure distribution, angles of attack of 6° and 11° were considered. By means of the display variant of vector fields in Ansys Fluent, the direction and height of the respective velocity vector can be visualised.

Fig. 8 shows the velocity field on the airfoil at 6° angle of attack. A thin, laminar boundary layer with low velocity (in blue) can be seen along the profile. Due to the abruptly ending trailing edge of the wing, backflows occur at this point. On modern airfoils, the reverse flows are reduced by tapering the trailing edge of the airfoil.

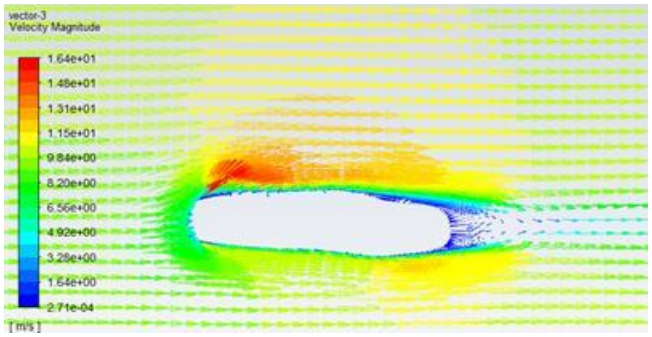

Fig. 8. Flow-field on the wing (α = 6°)

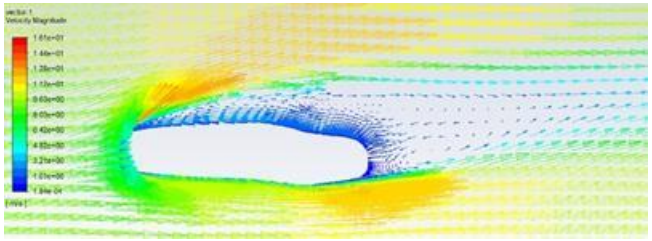

Fig. 9. Flow-field on the wing (α = 11°)

At an angle of attack of 11°, detachment of the boundary layer can be seen (s. fig. 9). The separation extends to the leading edge of the wing. Low flow velocities and the reverse flows reduce the effective lift, which can also be seen from the polars in Figs 2 and 3. A flight with an angle of attack of 11° is therefore not possible. With modern airfoils, flight at this angle of attack is usually possible, so that higher lift coefficients can also be achieved as a result of the higher angle of attack.

The flow separation phenomena are mainly favoured by the airfoil shape of the artefact, which does not have the characteristics of modern airfoils. It can be assumed that the airfoil shape was chosen to be approximately rectangular for manufacturing reasons. Removal of the leading and trailing edges due to the long-lasting weathering of the artefact is also conceivable.

4. CONCLUSION

Due to the poor aerodynamic characteristics of the studied artefact, it cannot be confirmed within the scope of this study that the “Bird of Saqqara” is a product of ancient aerodynamic knowledge. The artefact has a very high parasite drag with only low lift at the same time. In addition, the pressure distribution, as well as the location of the centre of gravity and aerodynamic centre (with respect to each other) suggest poor flight stability characteristics. A straight trajectory is therefore not possible. The artefact would perform an uncontrolled rolling motion, which in combination with the pitching moment would result in a stall. Even without considering the moment balance, the artefact does not have good gliding characteristics, which also excludes its use as a hand glider. Additionally, simple hand throwing tests would have been possible to perform in ancient Egypt and, with an understanding of aerodynamics, would have quickly revealed opportunities for optimisation.

Subsequent research should primarily focus on possible application within a cultural or religious context. The vertical tail fin could also be an indication of its suitability as a weathervane.

REFERENCES

1. Messiha K. African Experimental Aeronautics: A 2,000-Year-old model glider. Blacks in Science - Ancient and Modern. Ivan Van Sertima. 1991;92-97.
2. Schwarze R. CFD-Modellierung - Grundlagen und Anwendungen bei. Berlin Heidelberg New York. Springer-Verlag. 2012.
3. Abbott IH. Theory of Wing Sections. New York. Dover Publ. 1959.
4. Raymer DP. Aircraft Design - A Conceptual Approach. Stanford. Stanford University. American Institute of Aeronautics und Astronautics. 1989.
5. Sachs X, Hafer G. Flugmechanik - Moderne Flugzeugentwurfsund Steuerungskonzepte. Berlin Heidelberg New York. Springer-Verlag. 1993.
6. Hünecke K. Die Technik des modernen Verkehrsflugzeuges. Stuttgart. Motorbuch Verlag. 2017.

Michel Zierow: https://orcid.org/0000-0001-8724-972X
Leon Lesemann: https://orcid.org/0000-0002-2119-3134